Nonlinear Dyn (2023) 111:7525–7546
https://doi.org/10.1007/s11071-023-08250-y

ORIGINAL PAPER

# Two-dimensional composite multi-scale time–frequency reverse dispersion entropy-based fault diagnosis for rolling bearing

**Jiaqi Li · Jinde Zheng · Haiyang Pan · Jinyu Tong · Ke Feng · Qing Ni**

Received: 18 May 2022 / Accepted: 6 January 2023 / Published online: 23 January 2023


**Abstract** Multi-scale dispersion entropy ($MDE_{1D}$) is an effective nonlinear dynamic tool to characterize the complexity of time series and has been extensively applied to mechanical fault diagnosis. However, with the increase of scale factor, the values of $MDE_{1D}$ often fluctuate largely, resulting in poor stability. Besides, it only extracts the complexity information from the time domain of vibration signal, while the complexity information in the frequency domain is ignored. To enhance the stability of $MDE_{1D}$ and extract the complexity characteristics from the time–frequency domain of vibration signal, this paper first develops a two-dimensional multi-scale reverse dispersion entropy ($MRDE_{2D}$), inspired by the $MDE_{1D}$ and two-dimensional multi-scale dispersion entropy ($MDE_{2D}$) through introducing the "distance information from white noise". Then a two-dimensional multi-scale time–frequency reverse dispersion entropy ($MTFRDE_{2D}$) combined with time–frequency analysis is proposed. After that, considering that the length of the coarse-grained sequence used in the multi-scale coarse-grained process of $MTFRDE_{2D}$ will become shorter and shorter with the increase of scale factor, resulting in a loss of potentially useful information, the two-dimensional composite multi-scale time–frequency reverse dispersion entropy ($CMTFRDE_{2D}$) is proposed through using the composite coarse-grained process. The effectiveness and advantages of $CMTFRDE_{2D}$ algorithm are demonstrated by analyzing different kinds of noise signals. Following that, a new rolling bearing fault diagnosis method is proposed based on the $CMTFRDE_{2D}$ for feature extraction and gravitational search algorithm optimized support vector machine for mode identification. The proposed fault diagnosis method is employed on two rolling bearing test data sets and also compared with the existing $MTFRDE_{2D}$,- $MRDE_{2D}$,- $MDE_{2D}$,- and $MDE_{1D}$-based fault diagnosis methods. The analysis results reveal that the proposed fault diagnosis method can successfully extract the fault information from rolling bearing vibration signals in time–frequency domain and can accurately identify different fault locations and severities of rolling bearings with certain advantages.

**Keywords** Dispersion entropy · Two-dimensional multi-scale reverse dispersion entropy · Two-

J. Li · J. Zheng (✉) · H. Pan · J. Tong
School of Mechanical Engineering, Anhui University of Technology, Maanshan 243032, China
e-mail: lqdlzheng@126.com

J. Zheng
The State Key Laboratory of Mechanical Transmissions, Chongqing University, Chongqing, China

K. Feng
School of Engineering, University of British Columbia, British Columbia, Canada

Q. Ni
School of Mechanical and Mechatronic Engineering, University of Technology Sydney, Sydney, Australia

dimensional composite multi-scale time–frequency reverse dispersion entropy · Time–frequency distribution · Fault diagnosis

**Abbreviations**

| | |
|---|---|
| $ApEn_{1D}$ | Approximate entropy |
| $SampEn_{1D}$ | Sample entropy |
| $FE_{1D}$ | Fuzzy entropy |
| $PE_{1D}$ | Permutation entropy |
| $DE_{1D}$ | Dispersion Entropy |
| $RDE_{1D}$ | Reverse dispersion entropy |
| $MDE_{1D}$ | Multi-scale dispersion entropy |
| $MDE_{2D}$ | Two-dimensional multi-scale dispersion entropy |
| $MRDE_{2D}$ | Two-dimensional multi-scale reverse dispersion entropy |
| $MTFRDE_{2D}$ | Two-dimensional multi-scale time–frequency reverse dispersion entropy |
| $CMTFRDE_{2D}$ | Two-dimensional composite multi-scale time–frequency reverse dispersion entropy |
| SVM | Support vector machine |
| GSA | Gravitational search algorithm |
| PSO | Particle swarm optimization |
| CSO | Chicken swarm optimization |

## 1 Introduction

Thanks to the advantages of low friction resistance and high mechanical efficiency, rolling bearing performs an essential role in a range of industry applications. However, rolling bearing usually operates under harsh working environment, which makes it prone to failure. Hence, it is important significance to study the condition monitoring and early fault diagnosis approaches of rolling bearing [1].

As rolling bearing often presents non-stationary and nonlinear characteristics of vibration signal when local failure occurs in operation [2, 3], the traditional linear analysis methods inevitably have certain limitations. Therefore, the effective extraction of fault feature information hidden in the non-stationary and nonlinear signals becomes critical to rolling bearing fault diagnosis and prognosis.

Entropy index, including approximate entropy ($ApEn_{1D}$) [4], sample entropy ($SampEn_{1D}$) [5, 6], fuzzy entropy ($FE_{1D}$) [7], and permutation entropy ($PE_{1D}$) [8–10], has been recognized as a commonly-used nonlinear analysis tool which is widely used in feature extraction for rolling bearing, because of their stable and robust merits for relatively short data. $PE_{1D}$ is a nonlinear dynamic analysis to detect random changes in time series, which has the advantages of fast calculation speed and strong anti-noise ability. But the $PE_{1D}$ does not consider the relationship between the amplitudes of the original signal in the calculation process. Dispersion Entropy ($DE_{1D}$) has recently been proposed by Azami et al. [11, 12] for the measurement of complexity in time series to address the shortcomings of $PE_{1D}$. However, the stability of $DE_{1D}$ is poor and is easily affected by relevant parameters. Subsequently, the reverse dispersion entropy ($RDE_{1D}$) was proposed to improve the stability of $DE_{1D}$ by Li et al. [13], which is defined as "distance to white noise" and its better stability relative to $DE_{1D}$ was verified by the simulation tests and ship signals.

The above methods are all single-scale analysis tools based on entropy index, while the vibration signals usually contain different fault information in different scale ranges, thus the single-scale analysis tool still has some constraints to deal with these kinds of signals. The multi-scale dispersion entropy ($MDE_{1D}$) was proposed [14] to characterize the time series complexity on multiple time scales and applied to the field of biomedical signal analysis. However, $MDE_{1D}$ is defined on the one-dimensional time series and cannot be used to characterize the complexity characteristics of two-dimensional images. Recently, two-dimensional multi-scale dispersion entropy ($MDE_{2D}$) was proposed by Furlong et al. [15, 16] to characterize the complex characteristics of images in different scales.

$MDE_{1D}$ can only extract the time-domain characteristics of vibration signal, resulting in a loss and waste of the frequency domain information. $MDE_{2D}$ can effectively represent the complex characteristics of image, but the entropy value of $MDE_{2D}$ has poor stability and cannot provide stable and reliable analysis results. In this paper, first, the two-dimensional multi-scale reverse dispersion entropy ($MRDE_{2D}$) is proposed for solving the problem of $MDE_{2D}$ entropy values with poor stability. After that, the two-dimensional multi-scale time–frequency reverse dispersion entropy ($MTFRDE_{2D}$) is proposed by introducing time–frequency analysis [17, 18] for

measuring the complexity of the time–frequency distribution of vibration signals. However, as the coarse-grained sequence used in the multi-scale coarse-grained process of $MTFRDE_{2D}$ will become shorter in length with increasing scale factor, it will lose much potentially useful information. Then the two-dimensional composite multi-scale time–frequency reverse dispersion entropy ($CMTFRDE_{2D}$) is proposed to fully use the time–frequency distribution information of vibration signals on different scales. Finally, the effectiveness and superiority of $CMTFRDE_{2D}$ are verified by simulation signal analysis.

In general, the vibration signal of normal bearing, similar to white noise, is random with a high degree of irregularity. The vibration signal will become regular and periodic, impacted by the complexity change when the rolling bearing works with partial failures. In addition, the information of time–frequency distribution will also change with the increasing failure severity for the vibration signals usually contain different fault information in different scale ranges. Therefore, the proposed $CMTFRDE_{2D}$ method can be utilized to extract the time–frequency distribution information in different scales from the vibration signal of rolling bearings. After that, the gravitational search algorithm optimized support vector machine (GSA-SVM) is used for pattern recognition of fault features to achieve intelligent diagnosis of rolling bearing. According to the above analysis, a rolling bearing fault diagnosis method is proposed based on the $CMTFRDE_{2D}$ and GSA-SVM. The validity and advantages of the proposed fault diagnosis method are illustrated through two groups of rolling bearing test data under different operating conditions.

The major contributions of this paper are as follows:

(1) $CMTFRDE_{2D}$ is proposed to extract the fault features of the time–frequency distribution of vibration signals, which overcomes the defect that traditional entropy only extracts the time-domain features.
(2) In $CMTFRDE_{2D}$, the information utilization of the original signal is effectively improved by using the coarse-grained process of the moving average of adjacent elements.
(3) A rolling bearing fault diagnosis method is proposed based on the $CMTFRDE_{2D}$ and GSA-SVM, and the validity and superiority of the proposed method are verified by two sets of measured data.

This paper is structured as follows. In Sect. 2, the algorithms of $RDE_{2D}$ and $MRDE_{2D}$ are reviewed firstly and then the $CMTFRDE_{2D}$ algorithm is introduced, as well as the parameters selection of $RDE_{2D}$ and the performance of $CMTFRDE_{2D}$ are investigated. In Sect. 3, a new rolling bearing fault diagnosis method is proposed based on $CMTFRDE_{2D}$ and GSA-SVM. In Sect. 4, the effectiveness of the proposed fault diagnosis methods is verified by two sets of rolling bearing test data with different operating conditions. Finally, the discussion of conclusions is presented in Sect. 5.

## 2 $CMTFRDE_{2D}$ and its related algorithms

### 2.1 $RDE_{2D}$ algorithm

$DE_{2D}$ is a nonlinear analysis tool that can effectively characterize the complexity of images, but it has poor stability. In this paper, $RDE_{2D}$ is proposed by introducing "distance information from white noise" to improve the stability of $DE_{2D}$, and its steps can be described as follows:

(1) For a given image signal $U$ with pixel size $h \times w$, its discrete form is denoted as the matrix $U = \{u_{i,j}\}_{i=1,2,\cdots,h}^{j=1,2,\cdots,w}$. First, $U$ is mapped to $Y = \{y_{i,j}\}_{i=1,2,\cdots,h}^{j=1,2,\cdots,w}$ by utilizing the normal cumulative distribution function, namely

$$y_{i,j} = \frac{1}{\sigma\sqrt{2\pi}} \int_{-\infty}^{u_{i,j}} \frac{e^{-(t-\mu)^2}}{2\sigma^2} dt \tag{1}$$

where $\sigma$ and $\mu$ are the standard deviation and mean value of $U$, respectively. The range of $y_{i,j}$ is [0,1].

(2) A linear operation is used to map $y_{i,j}$ to the symbol sequence $z_{i,j}^c$, that is

$$z_{i,j}^c = \mathrm{int}(c \times y_{i,j} + 0.5) \tag{2}$$

where ***int***$(\cdot)$ indicates the rounding process, and $c$ is a positive integer, indicating the number of classes. $z_{i,j}^c$ stands for the class sequence of $i$-th

row and $j$-th column elements mapped from the element $u_{i,j}$ of image $U$.

(3) Based on the embedding theory, the embedding matrix is reconstructed as:

$$z^m = \left\{ z^{m,c}_{d,r} \right\} = \begin{bmatrix} z^c_{d,r} & z^c_{d,r+1} & \cdots & z^c_{d,r+(m_w-1)} \\ z^c_{d+1,r} & z^c_{d+1,r+1} & \cdots & z^c_{d+1,r+(m_w-1)} \\ \vdots & \vdots & \vdots & \vdots \\ z^c_{d+(m_h-1),r} & z^c_{d+(m_h-1),r+1} & \cdots & z^c_{d+(m_h-1),r+(m_{w-1})} \end{bmatrix} \tag{3}$$

where $m$ is embedding dimension, $1 \le d \le h - (m_h - 1)$ and $1 \le r \le w - (m_w - 1)$. For each element in $z^m$ is mapped to a dispersion pattern $\boldsymbol{\pi} = \pi_{x_0 x_1 \cdots x_{m_h \times m_{w-1}}}$, where $z^c_{d,r} = x_0$, $z^c_{d,r+1} = x_1, \ldots,$ $z^c_{d+(m_h-1),r+(m_w-1)} = x_{m_h \times m_w - 1}$. Since there are $m_h \times m_w$ elements in the matrix, and each element is mapped between 1 and $c$, there are total $\boldsymbol{q} = c^{m_h \times m_w}$ possible dispersion patterns corresponding to $z^m$.

(4) The probability $p(\boldsymbol{\pi})$ of each potential dispersion pattern in all possible dispersion patterns $\boldsymbol{q}$ can be computed by:

$$p(\boldsymbol{\pi}) = \frac{\text{number}\left\{ z^{m,c}_{d,r} \text{ has type } \boldsymbol{\pi} \right\}}{(h - (m_h - 1))(w - (m_w - 1))} \tag{4}$$

where ***number***$\{\cdot\}$ indicates the number of $z^{m,c}_{d,r}$ mapped to dispersion pattern $\pi$. In fact, $p(\boldsymbol{\pi})$ is equal to the ratio of the number of $z^{m,c}_{d,r}$ mapped to the dispersion pattern $\boldsymbol{\pi}$ to the total number $(h - (m_h - 1))(w - (m_w - 1))$ of all embedded vectors in $z^m$.

(5) $\text{RDE}_{2D}$ is defined as the distance to white noise by combining distance information as:

$$\begin{aligned} \text{RDE}_{2D}(U, m, c) &= \sum_{\pi=1}^{\boldsymbol{q}} \left( p(\boldsymbol{\pi}) - \frac{1}{\boldsymbol{q}} \right)^2 \\ &= \sum_{\pi=1}^{\boldsymbol{q}} p(\boldsymbol{\pi})^2 - \frac{1}{\boldsymbol{q}} \end{aligned} \tag{5}$$

There are two key parameters in $\text{RDE}_{2D}$ that are required to be set in advance, i.e., embedding dimension $m$ and class $c$. In the literature [15], it is suggested that $m$ is set from 1 to 5, and $c$ is set from 3 to 8. Generally, the larger $m$ is, the subtle changes cannot be accurately reflected in the joint probability dynamic reconstruction of the sequence, and the computation time is longer. To balance the accuracy and computation efficiency, $m = 2$ is chosen in this paper.

In the following, a $\text{MIX}_{2D}(n)$ function composed of periodic signals and random signals regulated by different probabilities $n$ $(0 \le n \le 1)$ was defined to verify the performance of $\text{RDE}_{2D}$ in detecting the degree of image irregularity and investigate the effect of $c$ on $\text{RDE}_{2D}$, where the $\text{MIX}_{2D}(n)$ is defined as below [19]

$$\text{MIX}_{2D}(n)_{i,j} = (1 - N_{i,j}) X_{i,j} + N_{i,j} Y_{i,j} \tag{6}$$

where the sinusoidal image $X_{i,j} = \sin(\frac{2\pi i}{12}) + \sin(\frac{2\pi j}{12})$, random image $Y_{i,j}$ consists of uniform white noise in the range $[-\sqrt{3}, \sqrt{3}]$. When the random variable $N_{i,j} = 1$, the probability is $n$, while when $N_{i,j} = 0$ the probability is $1 - n$. In fact, when the probability $n$ takes any value in the range, the $\text{MIX}_{2D}(n)$ generates an image that presents a specific spatial regularity. For example, when $n = 0$, $\text{MIX}_{2D}(n)$ generates regular periodic images. With the increase of probability $n$ $(0 \le n \le 1)$, the irregularity of the image generated by $\text{MIX}_{2D}(n)$ gradually increases, and a completely random and highly irregular image is generated when $n = 1$.

For different probability $n$, the $\text{MIX}_{2D}(n)$ randomly generates synthetic images with different regularity (as shown in Fig. 1), and its $\text{RDE}_{2D}$ value is computed and the entropy value curve is displayed in Fig. 2. As seen in Fig. 2, with the increasing of $n$ value, the irregularity of the image generated by $\text{MIX}_{2D}(n)$ will become higher and higher. Since the reverse dispersion entropy (or $\text{RDE}_{2D}$) is defined as the distance to white noise (or random image), the $\text{RDE}_{2D}$ values will become smaller with the increase of the image irregularity. Therefore, the trend of $\text{RDE}_{2D}$ is in line with the expected effect and corresponds to the image shown in Fig. 1, which further verifies the effectiveness of $\text{RDE}_{2D}$ in measuring the degree of image irregularity. In addition, Fig. 2 indicates that the value of entropy tends to decrease with the increase of $c$, and the entropy difference between different $n$ becomes smaller and smaller, which is not conducive to classification. It also can be observed from Fig. 2 that when $c = 3$, the difference of $\text{RDE}_{2D}$ value for different noises is the largest, and thus we set $c = 3$.

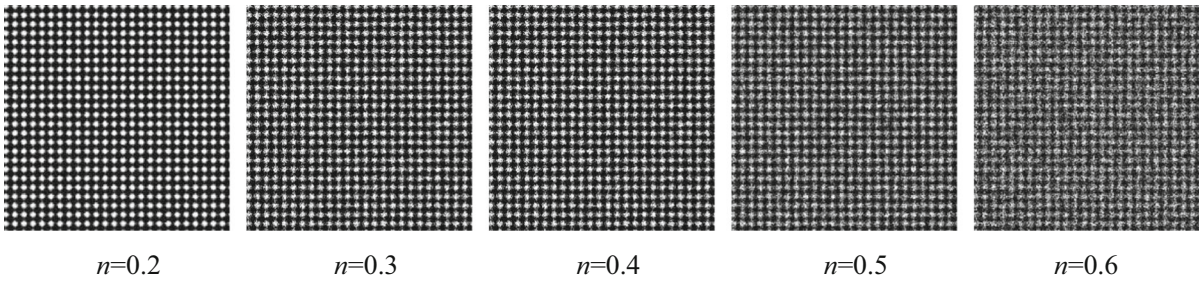


**Fig. 1** Composite image generated by $\mathrm{MIX}_{2D}(n)$ for different $n$ values

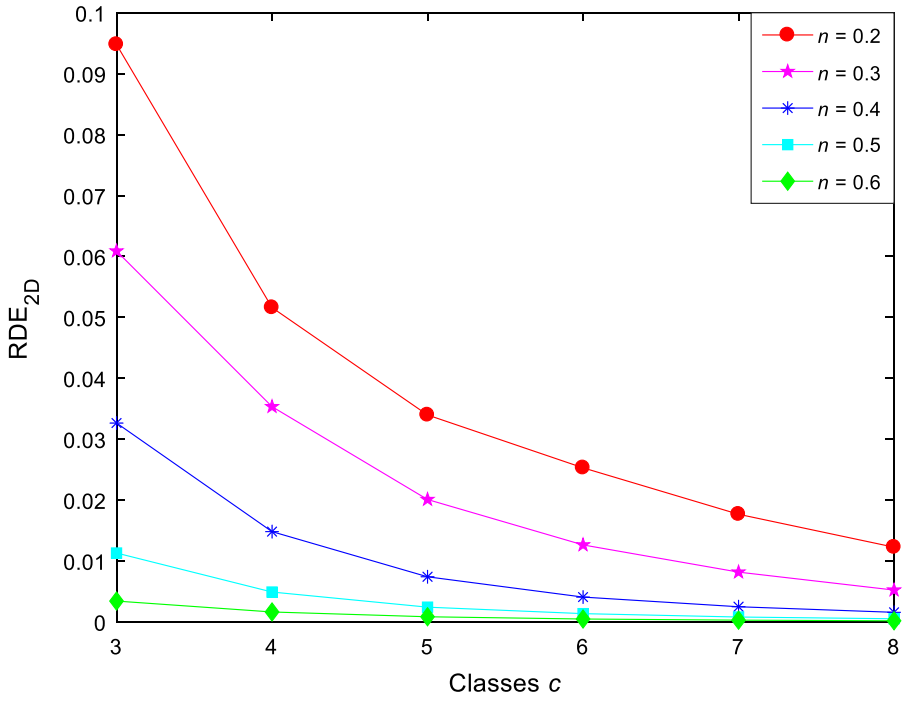


**Fig. 2** $\mathrm{RDE}_{2D}$ for different $n$ values

### 2.2 *MRDE$_{2D}$ algorithm*

Since the fault information is usually distributed on different time scales, accordingly, the complexity of image will change on different scales. In this part, $\mathrm{MRDE}_{2D}$ is proposed to reflect the complexity information of image on different scales, with its steps being described as follows.

(1) For image $U$ with size $h \times w$ and given scale factor of $\tau$, the size of the resulting coarse-grained image is $\lfloor h/\tau \rfloor \times \lfloor w/\tau \rfloor$, where $\lfloor \cdot \rfloor$ denotes rounding. The two-dimensional coarse-grained process of image is described by:

$$y_{i,j}^{(\tau)} = \frac{1}{\tau^2} \sum_{\substack{e=(i-1)\tau+1 \\ f=(j-1)\tau+1}}^{\substack{e=i\tau \\ f=j\tau}} x_{e,f},\ 1 \le i \le \lfloor h/\tau \rfloor,\ 1 \le j \le \lfloor w/\tau \rfloor \tag{7}$$

(2) For the coarse-grained image $y^{(\tau)} = \left\{ y_{i,j}^{(\tau)} \right\}$ with different scale factors $\tau$, $\mathrm{MRDE}_{2D}$ is defined by:

$$\mathrm{MRDE}_{2D}(U, \tau, m, c) = \mathrm{RDE}_{2D}\left( y^{(\tau)}, m, c \right) \tag{8}$$

$\mathrm{MRDE}_{2D}$ overcomes the problem that $\mathrm{RDE}_{2D}$ can only extract the complexity of single scale time series.

It extends the traditional coarse-grained method to a two-dimensional coarse-grained way which is applicable to image processing, and multi-scale image analysis has been developed to characterize the degree of irregularity of images for different scales. The schematic diagram of the two-dimensional coarse-grained for scale factor $\tau = 2$ is displayed in Fig. 3.

Although $\mathrm{MRDE}_{2D}$ overcomes the shortcomings of $\mathrm{RDE}_{2D}$ cannot perform multi-scale analysis of images, the coarse-grained process of $\mathrm{MRDE}_{2D}$ for images is relatively complex and computationally expensive. In addition, $\mathrm{MDE}_{1D}$ cannot comprehensively utilize the information in the time–frequency domain of vibration signals. Therefore, the $\mathrm{MTFRDE}_{2D}$ method is proposed, which combines the advantages of $\mathrm{MRDE}_{2D}$ and $\mathrm{MDE}_{1D}$ to extract the time–frequency distribution information of vibration signals. However, as the length of the coarse-grained sequence utilized in the multi-scale coarse-grained process of $\mathrm{MTFRDE}_{2D}$ will become shorter with the increase of scale factor, which inevitably leads to the loss of much potentially useful information. To address this issue, the $\mathrm{CMTFRDE}_{2D}$ method is proposed for solving the problem of information loss caused by $\mathrm{MTFRDE}_{2D}$.

### 2.3 Introduction of $\mathrm{CMTFRDE}_{2D}$ algorithm

The steps of the $\mathrm{CMTFRDE}_{2D}$ algorithm are given as follows.

(1) For a given scale factor $\tau$, the $n$-th $(1 \le n \le \tau)$ coarse-grained sequence $y_n^{(\tau)} = \{y_{n,1}^{(\tau)}, y_{n,2}^{(\tau)}, \cdots\}$ of the original time series $\{x(s), s = 1, 2, \cdots, S\}$ is defined as:

$$y_{n,j}^{(\tau)} = \frac{1}{\tau} \sum_{s=n+(j-1)\tau}^{j\tau+n-1} x_s, \ 1 \le j \le S/\tau, \ 1 \le n \le \tau \tag{9}$$

(2) For each coarse-grained sequence $y_n^{(\tau)}$ obtained when the scale factor is $\tau$, its time–frequency distribution $U_n^{(\tau)}$ is calculated through continuous wavelet transform, namely:

$$\begin{aligned} U(a,b) &= \int_{-\infty}^{+\infty} y_j^{(\tau)} \psi_{a,b}^* \, \mathrm{d}s \\ &= \frac{1}{\sqrt{a}} \int_{-\infty}^{+\infty} y_j^{(\tau)} \psi^* \left( \frac{s-b}{a} \right) \mathrm{d}s \end{aligned} \tag{10}$$

where $a$ is the scale and $a > 0$, $b$ represents the translation factor, $\frac{1}{\sqrt{a}}$ is the normalization factor in ensuring that $a$ and $b$ having the same energy, and $U(a,b)$ is the continuous wavelet transform of the coarse-grained time series $y_j^{(\tau)}$.

(3) For the time–frequency distribution $U_n^{(\tau)}$ of all coarse-grained sequences with scale factor $\tau$, its $\mathrm{CMTFRDE}_{2D}$ can be calculated by:

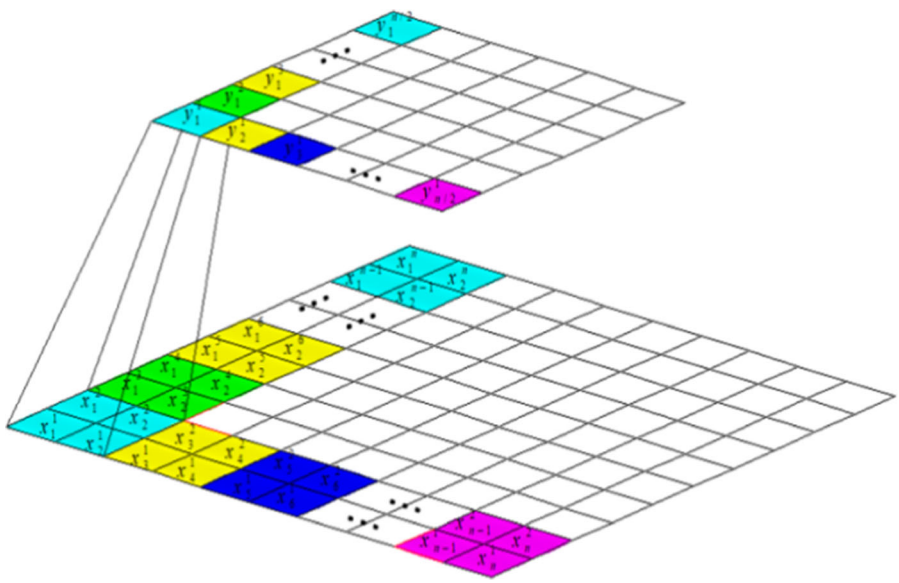

**Fig. 3** Schematic diagram of two-dimensional coarse-grained for $\tau = 2$

$$\mathrm{CMTFRDE_{2D}}(U,\tau,m,c) = \frac{1}{\tau}\sum_{n=1}^{\tau}\mathrm{RDE_{2D}}(U_n^{(\tau)},m,c) \quad (11)$$

The $\mathrm{CMTFRDE_{2D}}$ method reduces the fluctuation of entropy value with increasing scale factor by averaging $\mathrm{RDE_{2D}}$ values of $\tau$ coarse-grained sequence time–frequency images. Also, it can reduce the information loss caused by the coarse-grained process used in $\mathrm{MTFRDE_{2D}}$. Since $\mathrm{CMTFRDE_{2D}}$ is to calculate the $\mathrm{RDE_{2D}}$ values of the time–frequency distribution of composite coarse-grained time series, and thus the parameters settings are the same as $\mathrm{RDE_{2D}}$, i.e., $m = 2$ and $c = 3$ are set. The comparison of the computation process between $\mathrm{MRDE_{2D}}$ and $\mathrm{CMTFRDE_{2D}}$ is displayed in Fig. 4.

In the following, four kinds of noises, including pink noise, blue noise, purple noise, and red noise with a length of 1024, are selected as the research objects [20–22] to verify the effectiveness of $\mathrm{CMTFRDE_{2D}}$ in the complexity measurement of image and their waveforms in time-domain are exhibited in Fig. 5. The $\mathrm{CMTFRDE_{2D}}$, $\mathrm{MTFRDE_{2D}}$, $\mathrm{MRDE_{2D}}$ and $\mathrm{MDE_{2D}}$ values of the above noise signals with a maximum scale of $\tau_{\max} = 20$ were calculated [23], and the mean–variance diagram is displayed in Fig. 6. As seen in Fig. 5, the waveforms of pink noise and red noise are quite different that can be distinguished obviously, while the blue noise and purple noise waveforms are very similar and difficult to distinguish. The four different colored noises in the mean–variance diagram shown in Fig. 6 can be distinguished by the $\mathrm{CMTFRDE_{2D}}$ method, where the pink and red noises are more clearly distinguished from the other two noises, corresponding to the waveforms shown in Fig. 5, and thus the validity of the proposed method for feature extraction is confirmed. The standard

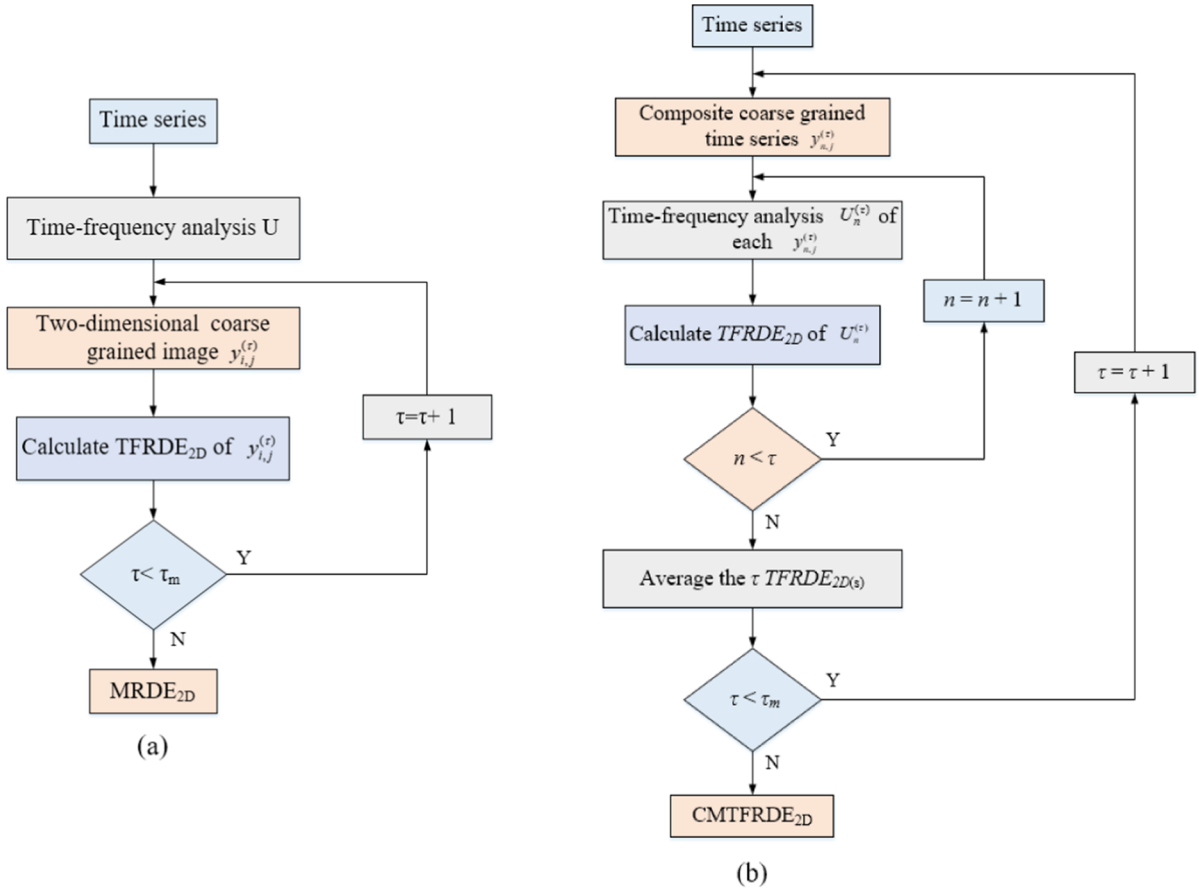


**Fig. 4** The flowcharts of $\mathrm{MRDE_{2D}}$ and $\mathrm{CMTFRDE_{2D}}$

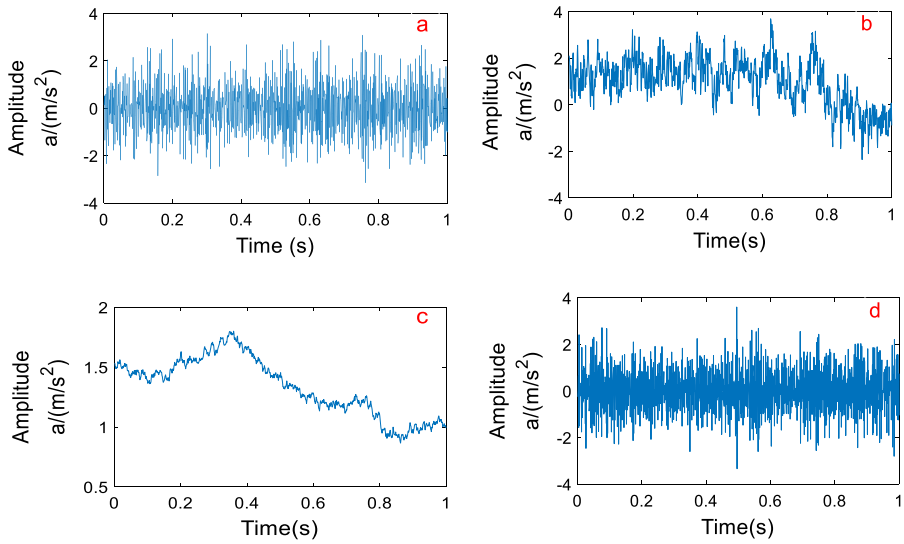


**Fig. 5** The colored noise waveform of (**a**) blue noise, (**b**) pink noise, (**c**) red noise, and (**d**) purple noise

deviation of the $CMTFRDE_{2D}$ method is the smallest among the four processing methods for different noise vibration signals, and this indicates that the $CMTFRDE_{2D}$ method has better stability and robustness in nonlinear dynamic feature reflection.

## 3 The proposed fault diagnosis method

The mentioned analysis demonstrates that $CMTFRDE_{2D}$ is an efficient method for vibration signals complexity analysis, which is used for feature extraction of rolling bearing vibration signals in this paper. However, it is essential to select an appropriate classifier to realize an intelligent fault classification of rolling bearing. Support vector machine (SVM) [24, 25] is a pattern recognition tool that is suitable for small sample classification, and its performance depends significantly on the selection of kernel parameter $g$ and penalty factor $c$. In general, $c$ is used to achieve a compromise between minimizing the number of misclassified samples and maximizing the classification interval. When the value of $c$ is small, the phenomenon of under-fitting occurs, which leads to lower training accuracy and poorer generalization performance. On the contrary, there will be an over-fitting phenomenon. And $g$ mainly affects the distribution of sample data in high-dimensional space, which also has a significant impact on the classification performance of SVM. However, the $c$ and $g$ value in SVM cannot be changed once determined. Therefore, the parameters of SVM need to be optimized to improve the classification efficiency. Particle swarm optimization (PSO) [26], chicken swarm optimization (CSO) [27] and gravitational search algorithm (GSA) [28, 29] are commonly used optimization algorithms. GSA is a cluster intelligence optimization algorithm with high robustness and easy implementation. The algorithm simulates the universal gravitational in physics, and the particles scattered in space move each other according to the gravitational interaction, and finally calculates the optimal position to realize position optimization. Therefore, the gravitational search algorithm is selected to optimize the relevant parameters of SVM in this paper.

### 3.1 Principle of gravitational search algorithm

GSA is a heuristic algorithm based on the law of universal gravitation. It can optimize the position of objects by simulating the interaction between objects with arbitrary mass to achieve the effect of parameter optimization. GSA needs to set parameters such as allowable range for search space, the maximum number of iterations and the number of agents in advance, and randomly initialize the positions of particles. Then the velocity, acceleration and position of the particle are updated according to formulas (12)–(15), and the iteration is stopped after the termination condition is satisfied, and the optimal parameters are output. The specific steps of GSA algorithm are described in the literature [30].

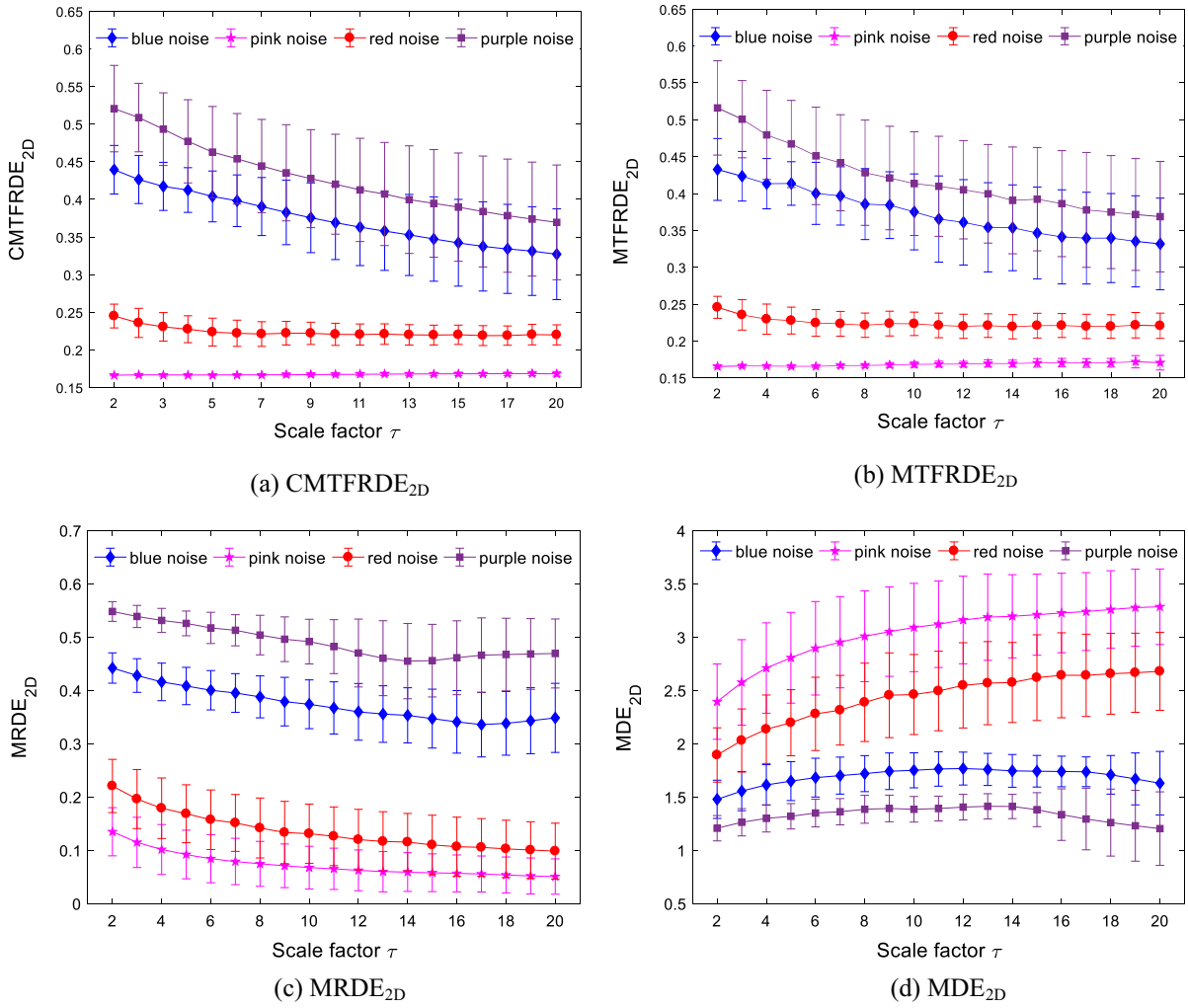


(a) $CMTFRDE_{2D}$ (b) $MTFRDE_{2D}$

(c) $MRDE_{2D}$ (d) $MDE_{2D}$

**Fig. 6** The mean standard deviation diagram of colored noise (**a**) $CMTFRDE_{2D}$, (**b**) $MTFRDE_{2D}$, (**c**) $MRDE_{2D}$ and (**d**) $MDE_{2D}$

$$F_{ij}^{l}(t) = G(t)\frac{M_{pi}(t) \times M_{dj}(t)}{R_{ij}(t) + \xi}(x_j^l(t) - x_i^l(t)) \tag{12}$$

$$a_i^l(t) = \frac{\sum_{j=1,j\neq i}^{N} rand_j F_{ij}^l(t)}{M_i(t)} \tag{13}$$

$$v_i^l(t+1) = rand_i \times v_i^l(t) + a_i^l(t) \tag{14}$$

$$x_i^l(t+1) = x_i^l(t) + v_i^l(t+1) \tag{15}$$

where $G(t)$ is the gravitational constant at time $t$, $M_{pi}(t)$ and $M_{dj}(t)$ are the gravitational masses of particles $i$ and $j$ respectively, $\xi$ is a small constant, $R_{ij}(t)$ is the Euclidean distance between particles $i$ and $j$, and $F_{ij}^l(t)$ is the resultant force of interaction between particles $i$ and $j$. $a_i^l(t)$ is the acceleration of particle $i$ in the $l$-th dimension, $M_i(t)$ is the inertial masses of particles $i$. $rand_j$ is a random variable between [0,1], $v_i^l(t)$ and $x_i^l(t)$ are the velocity and position of particle $i$ at the $t$-th iterations.

### 3.2 GSA-SVM optimization process

The penalty factor $c$ and the kernel parameter $g$ in the SVM are optimized using the GSA algorithm, and the specific steps are as follows:

(1) The parameters of GSA-SVM are initialized, i.e., the number of agents equals 20, the

maximum number of iterations is 30, the allowable range for search space is from 0.01 to 100, and randomly initialize position of particle.

(2) The minimum value of the objective function is used as the optimization target, and the fitness value of particle is calculated. It is worth noting that GSA-SVM takes the error rate between the actual output and the theoretical output of the test set as the fitness function, that is, the error rate of the classification prediction is used as the fitness value [31].

(3) The mass of each particle and the resultant force of interaction between particles are calculated.

(4) The velocity, acceleration and position of particle are updated, that is, the kernel parameter $g$ and penalty factor $c$ of SVM are updated.

(5) Repeat steps (2) $\sim$ (4) until the maximum number of iterations is achieved, and the iteration is terminated to output the optimal parameters.

### 3.3 The proposed method

Based on the advantages of $CMTFRDE_{2D}$ and GSA-SVM mentioned above, a new rolling bearing fault diagnosis model is proposed, and the detailed procedures are described as below.

(1) The vibration signals of rolling bearing are collected in $M$ different statues and each state contains $N$ samples with the same length. The $CMTFRDE_{2D}$ values for the time–frequency distribution of each state vibration signal with the maximum scale of $\tau_{max}$ are calculated and used being the sets of sample feature vectors.

(2) The sample feature vectors for each state vibration signal are divided randomly for $I$ training samples and $J$ testing samples, where $N = I + J$.

(3) The selected training samples are input to the GSA-SVM based classifier for training, in which GSA-SVM dynamically updates penalty factor $c$ and kernel parameter $g$ according to the different input training samples to obtain the optimal parameters.

(4) The testing samples are input into the GSA-SVM for classification prediction, and the fault locations and severities are judged according to the output results of classifier to achieve fault diagnosis of rolling bearing.

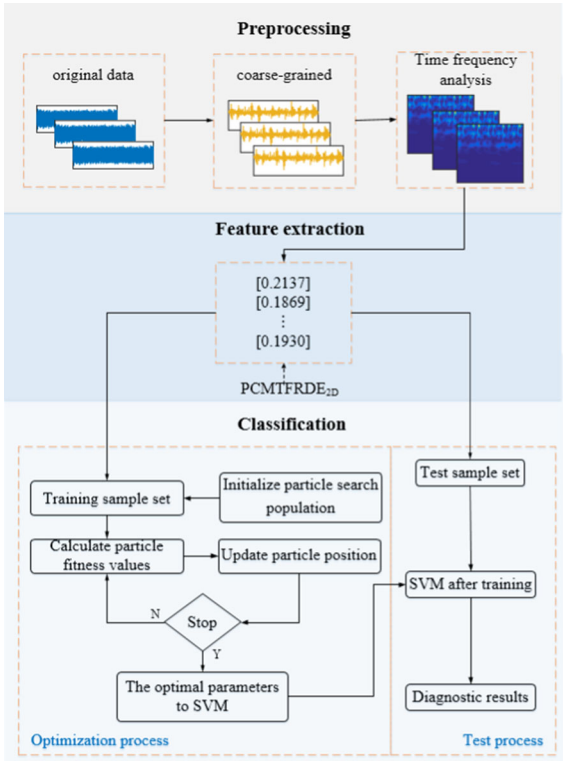


**Fig. 7** Flowchart of the proposed method

The process of the proposed fault diagnosis method is illustrated in Fig. 7.

## 4 Experimental data analysis

### 4.1 Experiment 1

The rolling bearing data of Case Western Reserve University[1] are employed to verify the validity of the proposed diagnosis method. The test bearing model used in the experiment is the 6205-2RSJEM SKF with a single point of failure assigned to the rolling bearing by EDM technology [32]. The test stand is displayed in Fig. 8. The vibration acceleration signals of rolling bearing with 12 different states were collected, respectively, under operating conditions with a

[1] https://github.com/yyxyz/CaseWesternReserveUniversityData.

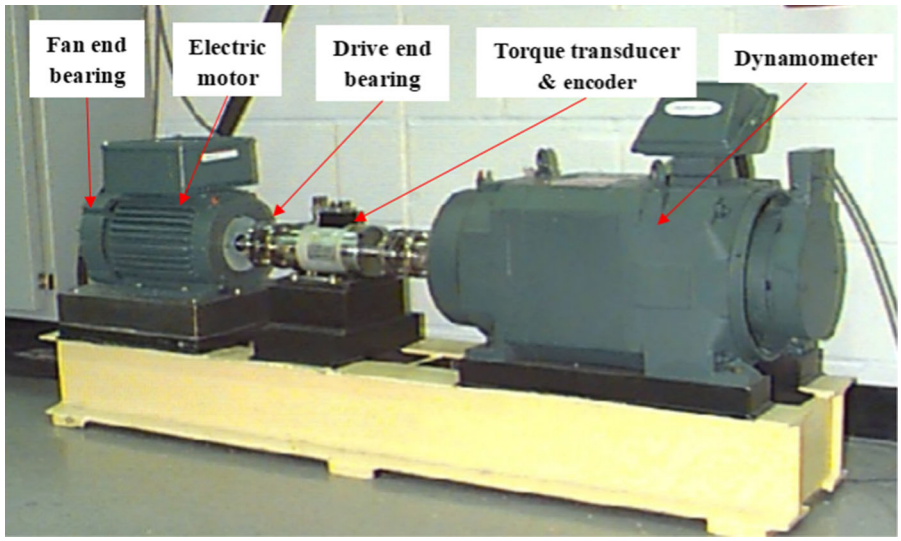


**Fig. 8** Case Western Reserve University bearing test bench

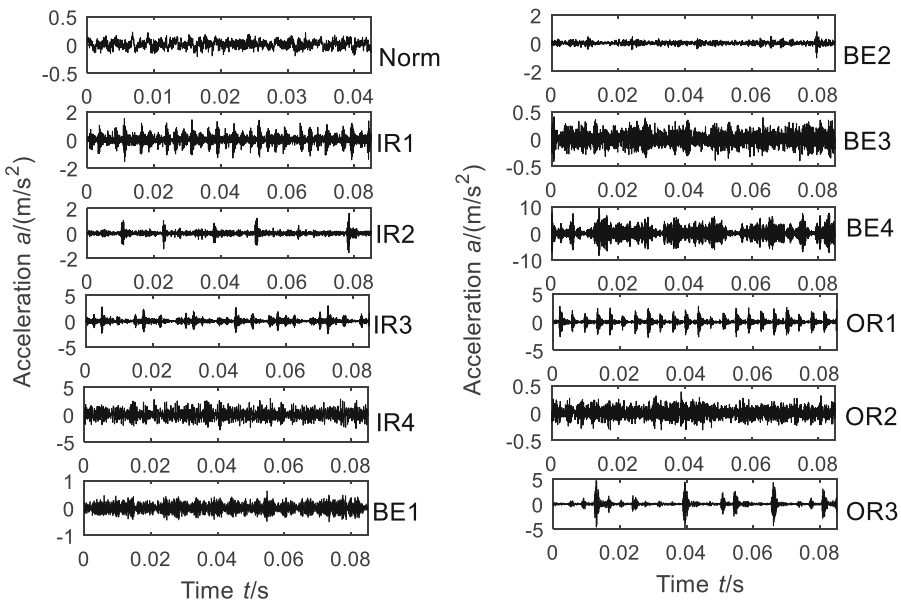


**Fig. 9** The time-domain waveforms of rolling bearing vibration signals

sampling frequency of 12 kHz and a speed of 1730 r/min, including normal bearing (denoted as Norm) and ball element fault, outer race fault and inner race fault bearings with fault diameters of 0.1778 mm, 0.3556 mm and 0.5334 mm, respectively, as well as ball element fault (BE4) and inner race fault (IR4) with fault diameter of 0.7112 mm. Among which ball element fault, outer race fault, and inner race fault with fault diameter of 0.1778 mm are denoted as BE1, OR1 and IR1, respectively. The bearings with fault diameter of 0.3556 mm are denoted as BE2, OR2 and IR2, and the bearings with fault diameter of 0.5334 mm are denoted as BE3, OR3 and IR3. The waveforms of vibration signals in time domain are shown in Fig. 9.

According to the proposed method, first, there are 30 samples with a length of 1024 collected from each of the above 12 states of rolling bearing vibration signal, and the $\mathrm{CMTFRDE}_{2D}$ value for time–frequency distribution with the maximum scale $\tau_{max} = 20$ of the collected data is calculated and the corresponding mean–variance diagram is present in Fig. 10a. According to Fig. 10a, the $\mathrm{CMTFRDE}_{2D}$

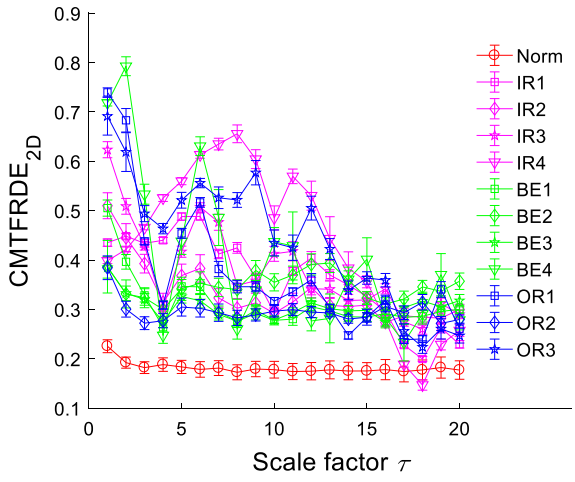


(a) $CMTFRDE_{2D}$

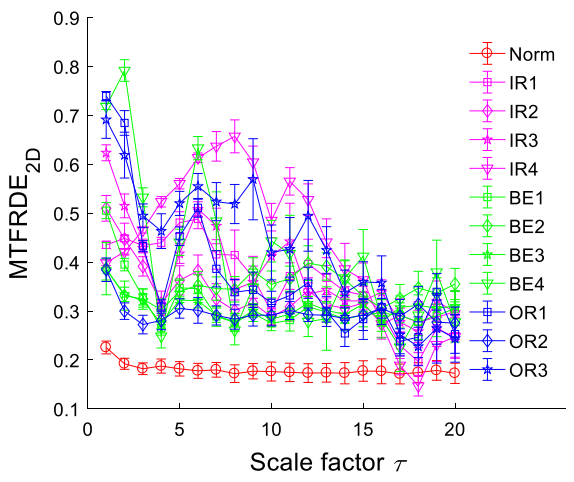


(b) $MTFRDE_{2D}$

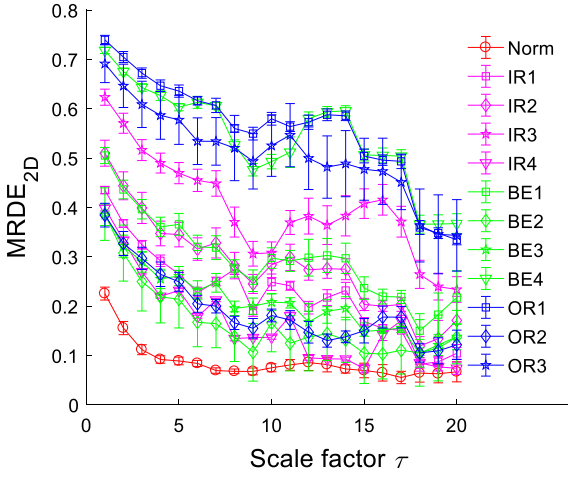


(c) $MRDE_{2D}$

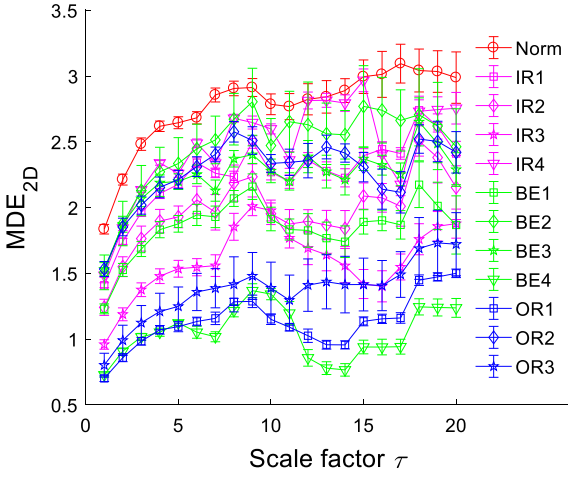


(d) $MDE_{2D}$

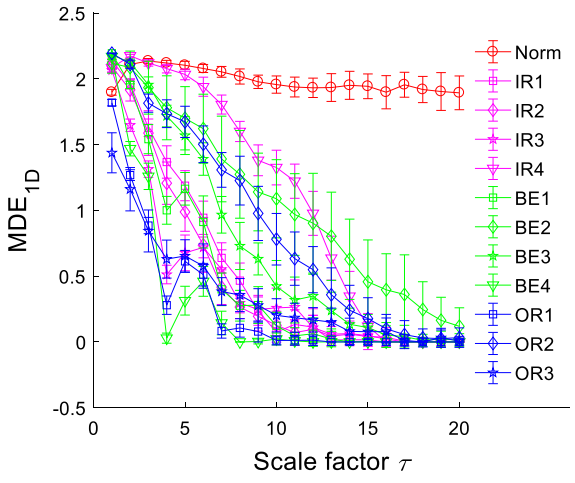


(e) $MDE_{1D}$

◀**Fig. 10** The mean standard deviation diagram of different processing methods (**a**) $CMTFRDE_{2D}$, (**b**) $MTFRDE_{2D}$, (**c**) $MRDE_{2D}$, (**d**) $MDE_{2D}$ and (**e**) $MDE_{1D}$

of rolling bearing vibration signals in 12 states decreases as the scale factor increases and can be effectively distinguished. In addition, the normal condition bearing has the smallest value of $CMTFRDE_{2D}$. This is because the resulting vibrations in rolling bearing during normal operation are random, the complexity of the signal is relatively large, and the corresponding entropy value is also large. The vibration generated will be accompanied by a certain periodic shock when the rolling bearing operates with local failure, resulting in the entropy being smaller than the normal state. However, reverse dispersion entropy is defined as the "distance from white noise" and thus the $CMTFRDE_{2D}$ is smallest when rolling bearings in normal conditions. The $CMTFRDE_{2D}$ value is larger for the vibration signal that has a periodic shock when the rolling bearing operates with local failure. In conclusion, $CMTFRDE_{2D}$ can effectively characterize the fault features of rolling bearing vibration signals.

Next, in order to demonstrate the advantages of $CMTFRDE_{2D}$ method, it is compared with $MTFRDE_{2D}$, $MRDE_{2D}$, $MDE_{2D}$ and $MDE_{1D}$ methods, respectively. The $MTFRDE_{2D}$, $MDE_{2D}$, $MRDE_{2D}$ and $MDE_{1D}$ values are calculated for the rolling bearing vibration signals (to make the test results not affected by the parameter settings, the parameter settings of $MTFRDE_{2D}$, $MRDE_{2D}$, $MDE_{2D}$ and $MDE_{1D}$ methods are the same as $CMTFRDE_{2D}$), and the mean standard deviation diagrams are shown in Fig. 10(b–e). Compared with Fig. 10(c and d), the $MRDE_{2D}$ and $MDE_{2D}$ curves show opposite trends, i.e., the $MDE_{2D}$ value for the vibration signal of rolling bearing gradually increases, while the $MRDE_{2D}$ value progressively decreases as the scale factor increases. The vibration signals of rolling bearings can be distinguished in different states by both methods. Besides, the standard deviation of the processing results of the $MRDE_{2D}$ method is smaller compared to the $MDE_{2D}$ method, which indicates that the $MRDE_{2D}$ method has stronger stability and robustness. As shown in Fig. 10(a and b), the two methods have similar trends, and the corresponding entropy values decrease gradually as the scale factor increases. The standard deviations of the $CMTFRDE_{2D}$ and $MTFRDE_{2D}$ are both smaller than those of the $MRDE_{2D}$ method, and the standard deviations of $CMTFRDE_{2D}$ values are smaller compared to those of $MTFRDE_{2D}$ as the scale factor increases. It reveals that the $CMTFRDE_{2D}$ method has better stability and reflects the advantages of composite multi-scale. In addition, the $MDE_{1D}$ curve of the bearing vibration signal in the normal state is clearly distinguished from that of the vibration signal in the faulty state, but when the scale factor is large, the $MDE_{1D}$ curve is not easy to differentiate for the faulty state rolling bearing vibration signal overlaps with each other. Moreover, the standard deviation of the $MDE_{1D}$ value is relatively large, and the stability is lower than the proposed method. In conclusion, the proposed $CMTFRDE_{2D}$ method can extract the time–frequency distribution information of rolling bearing vibration signal on different scales and has better stability.

To demonstrate the superiority of the proposed method in recognition accuracy, 10 samples are randomly chosen from the sample feature set of vibration signals in each state for training samples, and other 20 samples as testing sample sets and corresponding class labels are created. The classification labels are shown in Table 1. After that, the training samples are input into GSA-SVM to train, and the best kernel parameters and penalty factor obtained after training are 5.2282 and 34.8106, respectively. The testing samples are input into the trained multi-fault classifier to perform classification and the results are displayed in Fig. 11. By observing Fig. 11, it is found that the actual output result is exactly the same as the predicted result, with a recognition accuracy of 100%. Hence, the proposed $CMTFRDE_{2D}$ method can effectively extract the complex features for the time–frequency distribution of vibration signals, and the proposed fault diagnosis method can precisely recognize the different fault locations and severities of rolling bearings.

Further, the obtained $MTFRDE_{2D}$, $MRDE_{2D}$, $MDE_{2D}$, and $MDE_{1D}$ sample feature sets are input into GSA-SVM to train and test, with the test results being displayed in Fig. 12 and Table 2. By observing Fig. 12a–c, it is found that the diagnosis performance based on the $MRDE_{2D}$ method (5 samples are wrongly classified) is higher than that based on the $MDE_{2D}$ method (8 samples are wrongly classified), and the recognition accuracy is 97.92% and 96.67%,

**Table 1** Rolling bearing test data classification label

| Fault type | Fault diameter (mm) | No. of training samples | No. of testing samples | Class label |
|---|---|---|---|---|
| Norm | 0 | 10 | 20 | 1 |
| IR1 | 0.1778 | 10 | 20 | 2 |
| IR2 | 0.3556 | 10 | 20 | 3 |
| IR3 | 0.5334 | 10 | 20 | 4 |
| IR4 | 0.7112 | 10 | 20 | 5 |
| BE1 | 0.1778 | 10 | 20 | 6 |
| BE2 | 0.3556 | 10 | 20 | 7 |
| BE3 | 0.5334 | 10 | 20 | 8 |
| BE4 | 0.7112 | 10 | 20 | 9 |
| OR1 | 0.1778 | 10 | 20 | 10 |
| OR2 | 0.3556 | 10 | 20 | 11 |
| OR3 | 0.5334 | 10 | 20 | 12 |

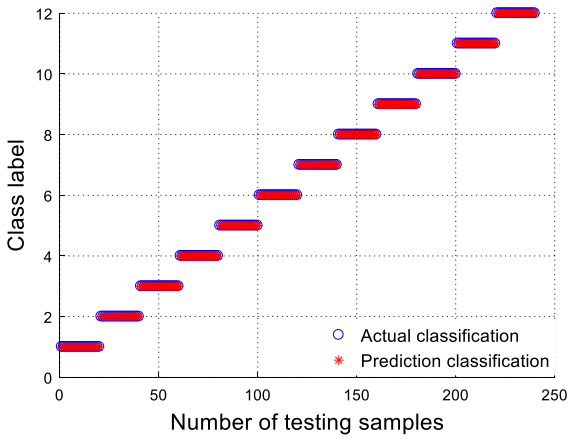


**Fig. 11** $CMTFRDE_{2D}$ classification results

respectively. Besides, the two samples in IR2 and one sample in OR2 are misjudged as BE1 and BE3 by the $MTFRDE_{2D}$ method, respectively. The identification accuracy is 98.75% which is higher than that of the $MRDE_{2D}$ method. From Fig. 12, it is found that the $MDE_{1D}$-based fault diagnosis method has the lowest recognition accuracy of 95.42%, with 11 samples being misjudged in total, which is lower than other two-dimensional entropy-based fault recognition methods, indicating that the two-dimensional entropy-based fault diagnosis method is better than the one-dimensional entropy method. In addition, these four methods of fault diagnosis all have different degrees of misjudgment, and their recognition accuracy is lower than that of the proposed method. Hence, the $CMTFRDE_{2D}$-based fault diagnosis method has certain superiority.

It is compared with PSO-SVM and CSO-SVM to verify the advantages of GSA-SVM in rolling bearing fault features pattern recognition. Without loss of generality, the same numbers of training samples and testing samples is used as above, and the corresponding classification results are listed in Table 2. From Table 2, it is found that PSO-SVM based on parameter optimization has the lowest identification rate for each feature set among the three parameters optimized classifiers. In contrast, the GSA-SVM has the highest recognition rate for each feature set, indicating that the GSA method can effectively avoid the local optimization situation and get relatively better parameter optimization results. Therefore, GSA-SVM has certain superiority in fault classification of rolling bearings.

Finally, the influence of input features number on the diagnosis results is investigated. Without loss of generality, the same number of training and testing samples are applied as in the above experiments. The first 15 sample features are sequentially input into GSA-SVM to train, and the recognition precision of the five methods is shown in Fig. 13. By observing Fig. 13, it is found that the identification accuracy of the $MDE_{1D}$-based method is always lower than the other four methods when the number of input samples is greater than 5, which is because the $MDE_{1D}$ method

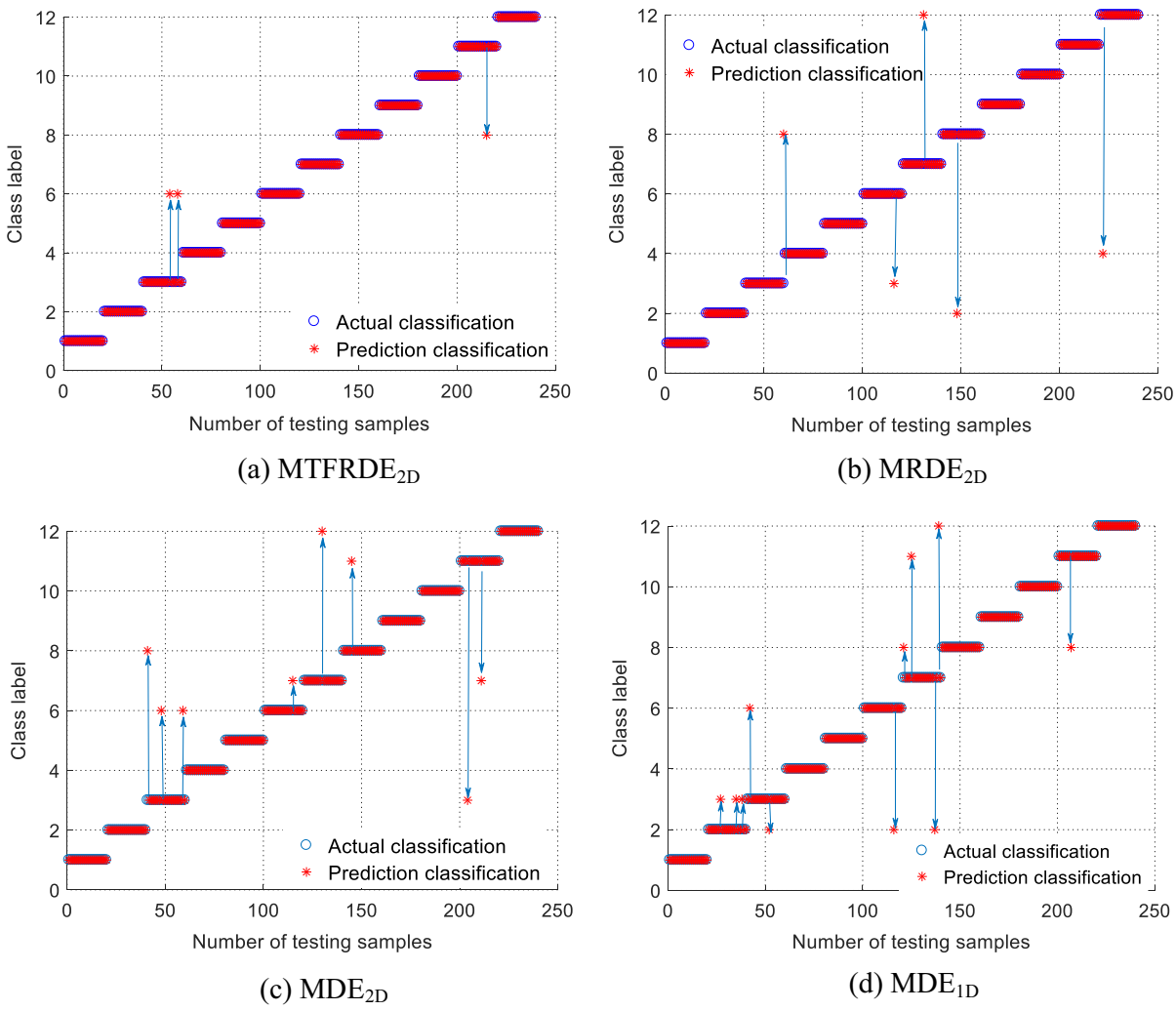


**Fig. 12** Classification results of different methods (a) $MTFRDE_{2D}$ (b) $MRDE_{2D}$ (c) $MDE_{2D}$ (d) $MDE_{1D}$

can only extract fault information in the time-domain with the incomplete fault information leading to the lowest recognition accuracy. In addition, the $CMTFRDE_{2D}$ method can always obtain the highest recognition accuracy compared with the other four methods regardless of the number of input features. Therefore, the proposed fault diagnosis method can also obtain higher recognition accuracy and has better robustness and stability when the number of input features is small.

In conclusion, the $CMTFRDE_{2D}$ method can effectively extract the fault characteristics from the time–frequency distribution of rolling bearings, and has better stability compared with the existing methods. The $CMTFRDE_{2D}$ and GSA-SVM-based fault diagnosis method can accurately identify the different health states of rolling bearings. In addition, the proposed method can obtain the highest recognition accuracy when the number of input sample features is small, which indicates that it is more suitable for small sample classification. Overall, the advantages of the proposed fault diagnosis methods mainly come from the fact that $CMTFRDE_{2D}$ can effectively improve the information utilization of the original signal, and the extracted features contain more fault information. Meanwhile, GSA-SVM can avoid the occurrence of local optimization in parameter optimization, thus improving the fault recognition rate of the diagnostic model.

**Table 2** Optimal parameters and recognition rate of five methods

| Method | | Parameter setting | Misclassified samples | Optimal parameters | Recognition rate (%) |
|---|---|---|---|---|---|
| **$CMTFRDE_{2D}$** | PSO-SVM | $m = 2$ | 4 | $c = 0.3603$, $g = 0.5502$ | 98.33 |
| | CSO-SVM | $c = 3$ | 1 | $c = 29.1305$, $g = 31.1103$ | 99.58 |
| | **GSA-SVM** | $\tau = 20$ | **0** | $\boldsymbol{c = 34.810}$, $\boldsymbol{g = 5.2282}$ | **100** |
| $MTFRDE_{2D}$ | PSO-SVM | | 6 | $c = 9.0233$, $g = 10.8914$ | 97.5 |
| | CSO-SVM | | 5 | $c = 11.9110$, $g = 7.3361$ | 97.92 |
| | GSA-SVM | | 3 | $c = 25.8862$, $g = 0.3501$ | 98.75 |
| $MRDE_{2D}$ | PSO-SVM | | 11 | $c = 100$, $g = 6.5340$ | 95.42 |
| | CSO-SVM | | 9 | $c = 76.6594$, $g = 1.1559$ | 96.25 |
| | GSA-SVM | | 5 | $c = 47.7172$, $g = 23.2000$ | 97.92 |
| $MDE_{2D}$ | PSO-SVM | | 12 | $c = 100$, $g = 2.2971$ | 95 |
| | CSO-SVM | | 10 | $c = 73.8741$, $g = 0.0100$ | 95.83 |
| | GSA-SVM | | 8 | $c = 69.0314$, $g = 2.1427$ | 96.67 |
| $MDE_{1D}$ | PSO-SVM | $m = 2$ | 17 | $c = 16.5803$, $g = 2.6305$ | 92.92 |
| | CSO-SVM | $c = 3$ | 12 | $c = 17.7283$, $g = 0.1323$ | 95 |
| | GSA-SVM | $d = 1$ | 11 | $c = 36.8317$, $g = 0.3473$ | 95.42 |
| | | $\tau = 20$ | | | |

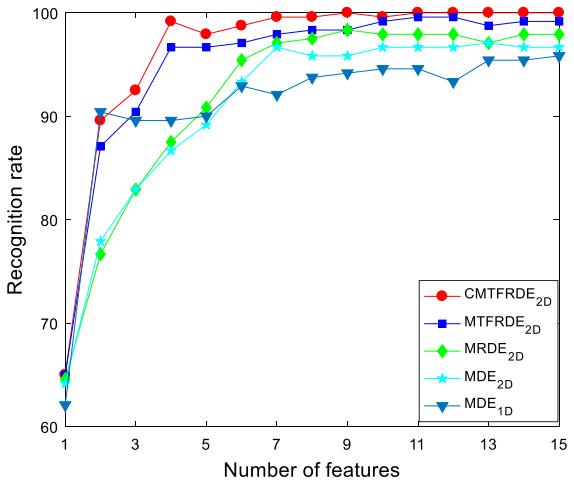


**Fig. 13** The recognition rate of five methods when inputting different feature numbers

## 4.2 Experiment 2

The test data obtained from the self-made rolling bearing simulation test rig is used for analyzing to further verify the superiority of the proposed method, and the simulation test rig as shown in Fig. 14. The test bearing type is SKF 6206-2Z, and the ball element fault (BE), outer race fault (OR), and inner race fault (IR) are arranged on the bearing utilizing wire cutting technology, respectively. The rolling bearing vibration acceleration signals of seven different fault depths were collected under the operating condition with a sampling frequency of 10.24 kHz, a motor speed of 1500 r/min, and a load of 7 kN. The specific description is shown in Table 3. Thirty samples with a length of 1024 are selected from each state rolling bearing vibration signal. The waveforms of the vibration signals in time-domain are shown in Fig. 15.

Firstly, the $CMTFRDE_{2D}$, $MTFRDE_{2D}$, $MRDE_{2D}$, $MDE_{2D}$, and $MDE_{1D}$ values of the above vibration signal with the maximum scale $\tau_{max} = 20$ are calculated, respectively, and other parameters settings are the same as those in Experiment 1. The mean standard deviation diagram of the corresponding entropy values is displayed in Fig. 16. As seen in Fig. 16, the overall change trends of $MRDE_{2D}$ and $MDE_{2D}$ are opposite as the scale factor increases, but the standard deviation of the $MRDE_{2D}$ processing results is smaller and has more excellent stability. Compared with the $MTFRDE_{2D}$, the $CMTFRDE_{2D}$ method has stronger stability and robustness, although the processing results of the two methods have similar trends.

A GSA-SVM multi-fault classifier is constructed to further demonstrate the advantages of the proposed

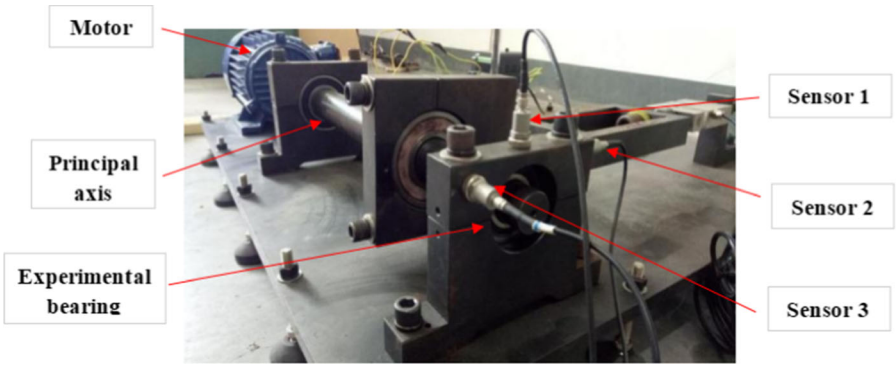


**Fig. 14** Self-made rolling bearing simulation test bench

**Table 3** Rolling bearing test data classification label

| Fault type | Fault size (mm) | No. of training samples | No. of testing samples | Class label |
|---|---|---|---|---|
| Norm | 0 | 10 | 20 | 1 |
| IR1 | 0.3 | 10 | 20 | 2 |
| IR2 | 0.4 | 10 | 20 | 3 |
| BE1 | 0.2 | 10 | 20 | 4 |
| BE2 | 0.4 | 10 | 20 | 5 |
| OR1 | 0.2 | 10 | 20 | 6 |
| OR2 | 0.3 | 10 | 20 | 7 |

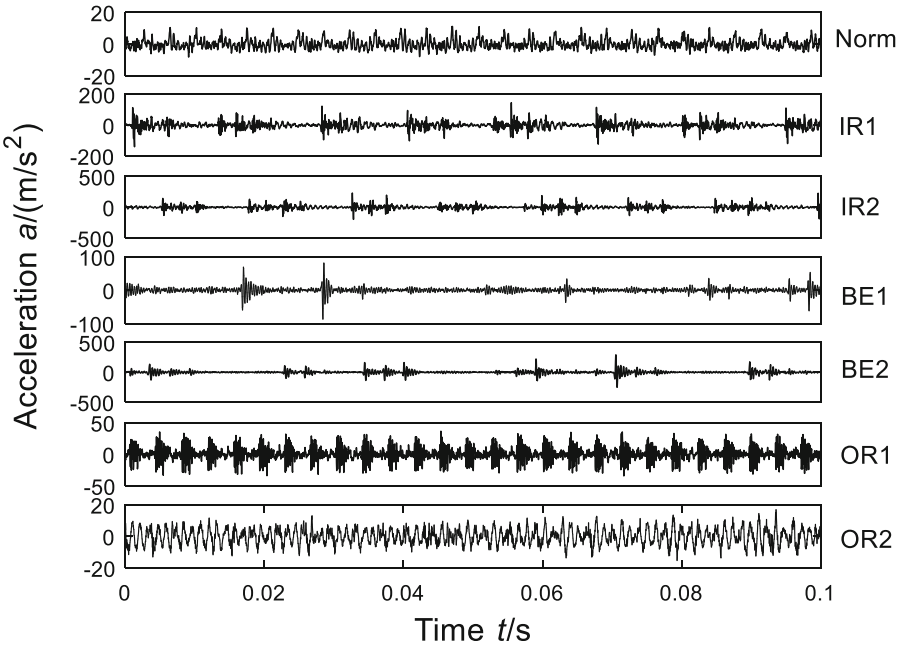


**Fig. 15** The time-domain waveform of rolling bearing vibration signals

fault diagnosis method in recognition accuracy. Without losing generality, the same number of training and testing samples as in Experiment 1, and the specific description is shown in Table 3. After that, the training and testing samples are input into GSA-SVM to perform prediction and classification, and the

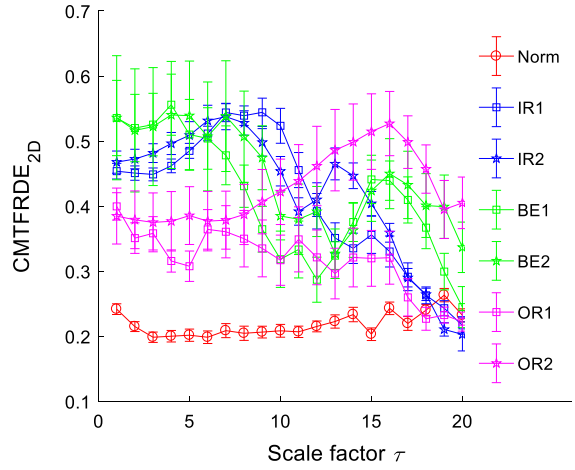


(a) $CMTFRDE_{2D}$

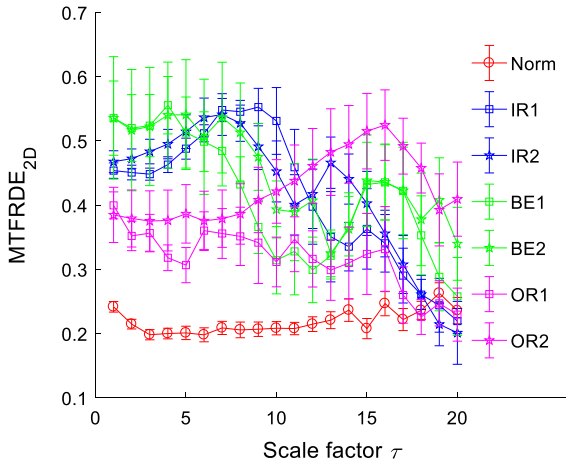


(b) $MTFRDE_{2D}$

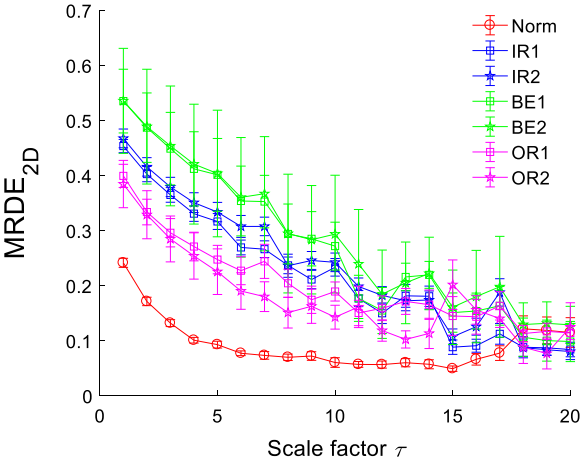


(c) $MRDE_{2D}$

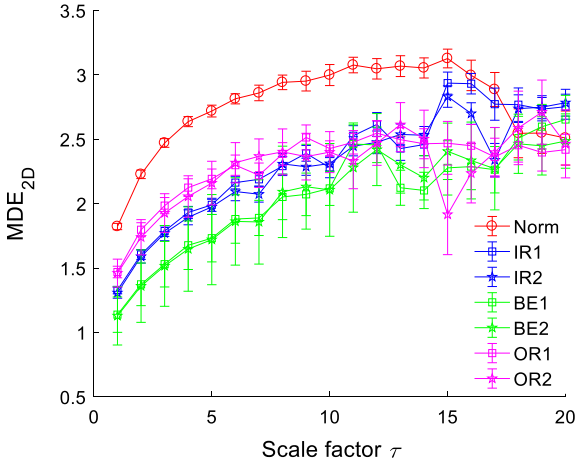


(d) $MDE_{2D}$

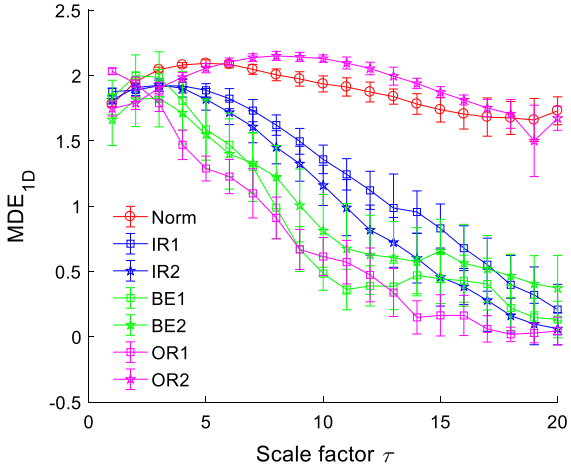


(e) $MDE_{1D}$

◀**Fig. 16** The mean standard deviation diagram of different processing methods (**a**) $CMTFRDE_{2D}$, (**b**) $MTFRDE_{2D}$, (**c**) $MRDE_{2D}$, (**d**) $MDE_{2D}$ and (**e**) $MDE_{1D}$

corresponding optimization parameters and output results are listed in Fig. 17 and Table 4, respectively. By observing Fig. 17 and Table 4, it is found that the proposed method correctly classifies the vibration signals of rolling bearings with different fault locations and severities, and the recognition accuracy is 100%. The $MTFRDE_{2D}$-based fault diagnosis method divides two samples of BE1 into BE2 by mistake with a recognition accuracy of 98.57%, which indicates that the $MTFRDE_{2D}$ method can accurately identify different fault locations, but the ability to distinguish different fault degrees of the same locations is lower than the proposed method. The fault diagnosis methods based on $MRDE_{2D}$, $MDE_{2D}$, and $MDE_{1D}$ all have different degrees of misjudgment, and the recognition accuracy is $MRDE_{2D}$, $MDE_{2D}$, and $MDE_{1D}$ in descending order. To sum up, the proposed $CMTFRDE_{2D}$-based fault diagnosis method has the highest recognition accuracy among the five different fault diagnosis methods and has certain advantages.

Next, compared with PSO-SVM and CSO-SVM to illustrate the advantage of the GSA-SVM classifier, the results are listed in Table 4. As demonstrated in Table 4, the GSA-SVM can achieve the highest recognition accuracy no matter which feature set is input among the three classifiers that optimized parameters based on different algorithms, which further verifies the superiority of the GSA-SVM in fault pattern identification.

Finally, the influence of the input features number on the classification results is investigated. The 30 samples of rolling bearing vibration signals in each state are divided randomly into 10 samples to train and the other 20 samples to test. The recognition accuracy obtained according to the different number of input features is displayed in Fig. 18. As demonstrated in Fig. 18, when the number of input features is small, the other four methods have poor classification results. While the recognition precision of the $CMTFRDE_{2D}$ method is higher than the other four methods regardless of the number of input features. In addition, when the number of input features is greater than 10, the recognition rate of the $CMTFRDE_{2D}$ method reaches and stabilizes at 100%. Combined with the analysis results of Experiment 1, it can be seen that better classification results can be obtained with the number of input features greater than 11. Therefore, the method of fault diagnosis based on $CMTFRDE_{2D}$ has more advantages in small sample classification.

## 5 Conclusion

In this paper, firstly, based on the definition of $MDE_{2D}$, the two-dimensional multi-scale reverse dispersion entropy ($MRDE_{2D}$) is proposed by introducing "distance information from white noise", and then the two-dimensional multi-scale time–frequency reverse dispersion entropy ($MTFRDE_{2D}$) is developed to quantify the complexity of time–frequency distribution information for vibration signal of rolling bearing. Based on that, the two-dimensional composite multi-scale time–frequency reverse dispersion entropy ($CMTFRDE_{2D}$) is proposed to reduce the information loss caused by conventional coarse-grained used in $MTFRDE_{2D}$, and to alleviate the phenomenon that the entropy value fluctuation of $MTFRDE_{2D}$ as the scale factor increases. The effectiveness and stability of the $CMTFRDE_{2D}$ for signal complexity measurement are verified through four kinds of colored noise analysis. After that, an intelligent diagnosis method of rolling bearing based on $CMTFRDE_{2D}$ and GSA-SVM is proposed, which is subsequently employed on rolling bearing test data under two different working conditions. The results reveal that the proposed method can accurately identify different locations and severities of faults in rolling bearings with greater robustness and stability than the $MTFRDE_{2D}$, $MRDE_{2D}$, $MDE_{2D}$, and $MDE_{1D}$ methods. In addition, the effect of the number of input features upon the classification results also is investigated. The results indicate that the proposed method still has high recognition precision with less input features, and it is found that a higher recognition rate can be achieved with a number of input features greater than 11. Finally, the superiority of GSA-SVM in fault pattern recognition is demonstrated by comparing it with several other most commonly employed optimization algorithms. In summary, the $CMTFRDE_{2D}$ and GSA-SVM-based rolling bearing fault diagnosis method can effectively extract the fault information of vibration signal and has a certain superiority over the compared methods in fault identification. However, the parameter selection of

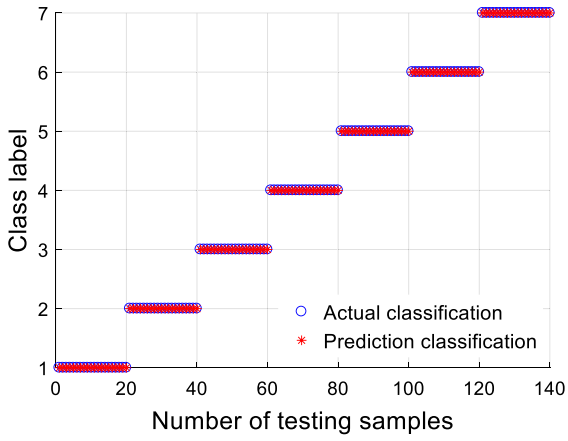


(a) $CMTFRDE_{2D}$

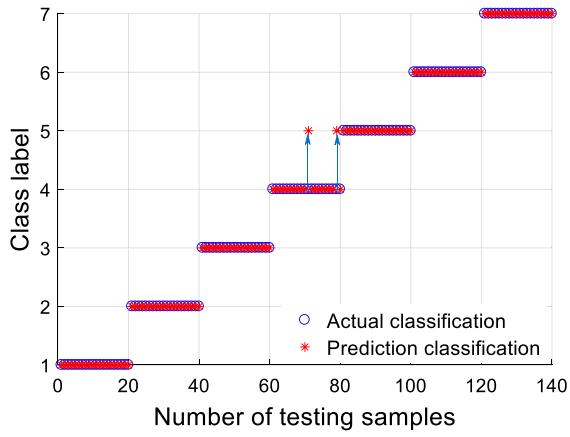


(b) $MTFRDE_{2D}$

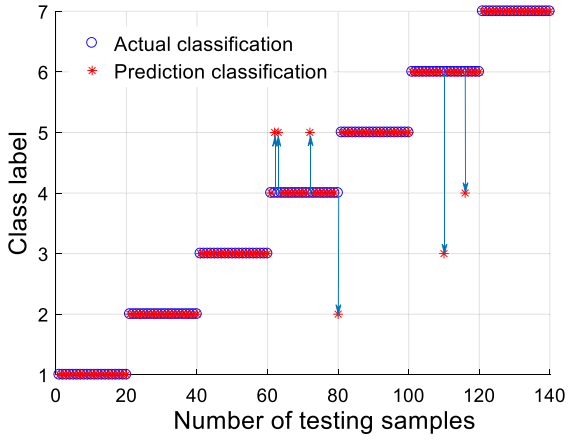


(c) $MRDE_{2D}$

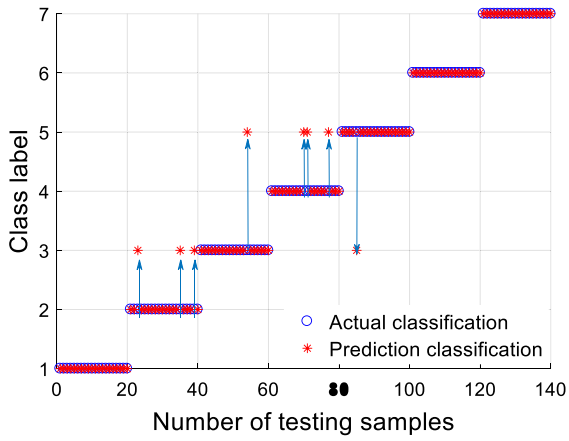


(d) $MDE_{2D}$

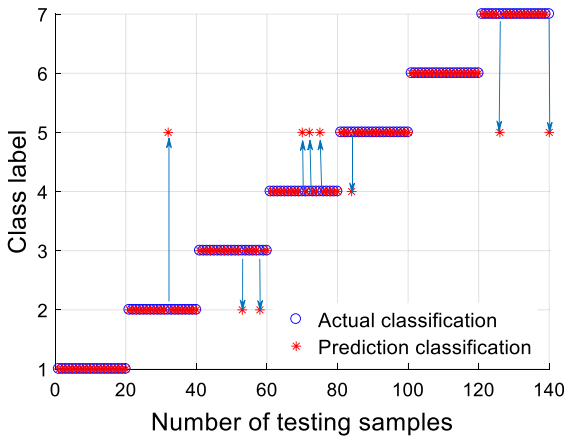


(e) $MDE_{1D}$

**Fig. 17** Classification results of different methods (**a**) $CMTFRDE_{2D}$, (**b**) $MTFRDE_{2D}$, (**c**) $MRDE_{2D}$, (**d**) $MDE_{2D}$ and (**e**) $MDE_{1D}$

**Table 4** Optimal parameters and recognition rate of five methods

| Method | Misclassified samples | Optimal parameters | Recognition rate (%) | |
|---|---|---|---|---|
| **$CMTFRDE_{2D}$** | PSO-SVM | 4 | $c$ = 7.7887, $g$ = 0.1340 | 97.14 |
| | CSO-SVM | 2 | $c$ = 61.9892, $g$ = 54.3217 | 98.57 |
| | **GSA-SVM** | **0** | ***c* = 74.9559, *g* = 32.7572** | **100** |
| $MTFRDE_{2D}$ | PSO-SVM | 5 | $c$ = 100, $g$ = 8.7604 | 96.43 |
| | CSO-SVM | 4 | $c$ = 62.0886, $g$ = 5.8180 | 97.14 |
| | GSA-SVM | 2 | $c$ = 79.0288, $g$ = 12.4137 | 98.57 |
| $MRDE_{2D}$ | PSO-SVM | 7 | $c$ = 100, $g$ = 73.9538 | 95 |
| | CSO-SVM | 6 | $c$ = 73.1461, $g$ = 1.2725 | 95.71 |
| | GSA-SVM | 6 | $c$ = 47.6383, $g$ = 7.9343 | 95.71 |
| $MDE_{2D}$ | PSO-SVM | 9 | $c$ = 10.3924, $g$ = 3.7516 | 93.57 |
| | CSO-SVM | 7 | $c$ = 24.1872, $g$ = 0.0967 | 95 |
| | GSA-SVM | 8 | $c$ = 19.3252, $g$ = 0.5365 | 94.29 |
| $MDE_{1D}$ | PSO-SVM | 13 | $c$ = 36.0234, $g$ = 4.9120 | 90.71 |
| | CSO-SVM | 11 | $c$ = 33.7191, $g$ = 1.5312 | 92.14 |
| | GSA-SVM | 9 | $c$ = 34.3364, $g$ = 2.1176 | 93.57 |

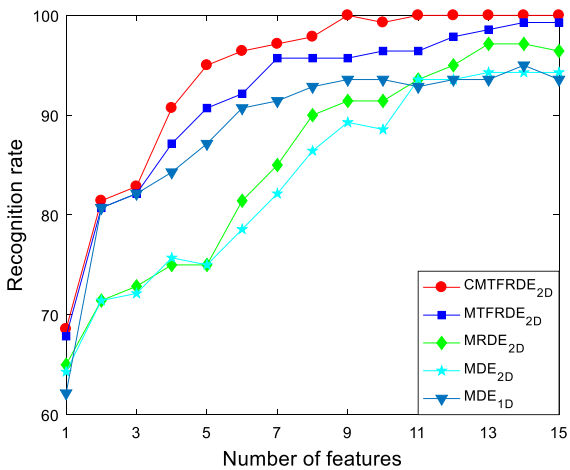


**Fig. 18** The recognition rate of five methods when inputting different feature numbers

$CMTFRDE_{2D}$ still requires to be studied in future work.

In fact, due to the influence of background noise and complex environment in practical engineering applications, it is not easy to effectively diagnose mechanical equipment in different health conditions without the given known knowledge. We want to say that this paper verifies the validity and superiority of the proposed method through the test data of rolling bearings under two different working conditions, which provides a new way for the fault diagnosis of mechanical equipment. In addition, we will apply the proposed method to the fault diagnosis of planetary gears and rotors in the future work to further study the application area of this method.

**Acknowledgements** This work was supported by the National Natural Science Foundation of China (No. 51975004), the Natural Science Foundation of Anhui Province of China (No. 2008085QE215), and the State Key Laboratory of Mechanical Transmissions (SKLMT-MSKFKT-202107).

**Data availability** The datasets generated during and/or analysed during the current study are available from the corresponding author on reasonable request.

**Declarations**

**Conflict of interest** The authors declare that they have no known competing financial interests or personal relationships that could have appeared to influence the work reported in this paper.

**Ethical approval** The authors declare that they have adhered to the ethical standards of research execution.

## References

1. Lin, J., Chen, Q.: Fault diagnosis of rolling bearings based on multifractal detrended fluctuation analysis and

Mahalanobis distance criterion. Mech. Syst. Signal Process. **38**(2), 515–533 (2013)
2. Zheng, J., Pan, H., Yang, S., et al.: Adaptive parameterless empirical wavelet transform based time-frequency analysis method and its application to rotor rubbing fault diagnosis. Signal Process. **130**, 305–314 (2017)
3. Feng, K., Wang, K., Ni, Q., et al.: A phase angle based diagnostic scheme to planetary gear faults diagnostics under non-stationary operational conditions. J. Sound Vib. **408**, 190–209 (2017)
4. Pincus, S.M.: Approximate entropy as a measure of system complexity. Proc. Natl. Acad. Sci. **88**(6), 2297–2301 (1991)
5. Richman, J.S., Moorman, J.R.: Physiological time-series analysis using approximate entropy and sample entropy. Am. J. Physiol. Heart Circ. Physiol. **278**(6), H2039–H2049 (2000)
6. Xiang, D., Ge, S.: A model of fault feature extraction based on wavelet packet sample entropy and manifold learning. J. Vib. Shock **33**(11), 1–5 (2014)
7. Zheng, J., Cheng, J., Yang, Y.: A rolling bearing fault diagnosis approach based on LCD and fuzzy entropy. Mech. Mach. Theory **70**, 441–453 (2013)
8. Bandt, C., Pompe, B.: Permutation entropy: a natural complexity measure for time series. Phys. Rev. Lett. **88**(17), 174102 (2002)
9. Kuai, M., Cheng, G., Pang, Y., et al.: Research of planetary gear fault diagnosis based on permutation entropy of CEEMDAN and ANFIS. Sensors **18**(3), 782 (2018)
10. Ying, W., Zheng, J., Pan, H., et al.: Permutation entropy-based improved uniform phase empirical mode decomposition for mechanical fault diagnosis. Digital Signal Process. **117**, 103167 (2021)
11. Rostaghi, M., Azami, H.: Dispersion entropy: a measure for time-series analysis. IEEE Signal Process. Lett. **23**(5), 610–614 (2016)
12. Rostaghi, M., Ashory, M.R., Azami, H.: Application of dispersion entropy to status characterization of rotary machines. J. Sound Vib. **438**, 291–308 (2019)
13. Li, Y., Gao, X., Wang, L.: Reverse dispersion entropy: a new complexity measure for sensor signal. Sensors **19**(23), 5203 (2019)
14. H. Azami, E. Kinney-Lang, A. Ebied et al. Multiscale dispersion entropy for the regional analysis of resting-state magnetoencephalogram complexity in Alzheimer's disease. In: 39th Annual International Conference of the IEEE Engineering in Medicine and Biology Society (EMBC). IEEE, (2017). pp 3182–3185.
15. Azami, H., Silva, L.E.V., Omoto, A.C.M., et al.: Two-dimensional dispersion entropy: an information-theoretic method for irregularity analysis of images. Signal Process. Image Commun. **75**, 178–187 (2019)
16. Furlong, R., Hilal, M., O'brien, V., et al.: Parameter analysis of multiscale two-dimensional fuzzy and dispersion entropy measures using machine learning classification. Entropy **23**(10), 1303 (2021)
17. Park, J., Kim, Y., Na, K., et al.: An image-based feature extraction method for fault diagnosis of variable-speed rotating machinery. Mech. Syst. Signal Process. **167**, 108524 (2022)
18. Al-Badour, F., Sunar, M., Cheded, L.: Vibration analysis of rotating machinery using time–frequency analysis and wavelet techniques. Mech. Syst. Signal Process. **25**(6), 2083–2101 (2011)
19. Silva, L.E.V., Senra Filho, A.C.S., Fazan, V.P.S., et al.: Two-dimensional sample entropy: assessing image texture through irregularity. Biomed. Phys. Eng. Express **2**(4), 045002 (2016)
20. Ahmed, A.G.M., Perrier, H., Coeurjolly, D., et al.: Low-discrepancy blue noise sampling. ACM Trans. Graph. (TOG) **35**(6), 1–13 (2016)
21. Hilal, M., Berthin, C., Martin, L., et al.: Bidimensional multiscale fuzzy entropy and its application to pseudoxanthoma elasticum. IEEE Trans. Biomed. Eng. **67**(7), 2015–2022 (2019)
22. Adamer, M.F., Harrington, H.A., Gaffney, E.A., et al.: Coloured noise from stochastic inflows in reaction–diffusion systems. Bull. Math. Biol. **82**(4), 1–28 (2020)
23. Zheng, J., Pan, H., Yang, S., et al.: Generalized composite multiscale permutation entropy and Laplacian score based rolling bearing fault diagnosis. Mech. Syst. Signal Process. **99**, 229–243 (2018)
24. Hu, X., Che, Y., Lin, X., et al.: Health prognosis for electric vehicle battery packs: A data-driven approach. IEEE/ASME Trans. Mechatron. **25**(6), 2622–2632 (2020)
25. Li, Y., Yang, Y., Wang, X., et al.: Early fault diagnosis of rolling bearings based on hierarchical symbol dynamic entropy and binary tree support vector machine. J. Sound Vib. **428**, 72–86 (2018)
26. Coello, C.A.C., Pulido, G.T., Lechuga, M.S.: Handling multiple objectives with particle swarm optimization. IEEE Trans. Evol. Comput. **8**(3), 256–279 (2004)
27. Deb, S., Gao, X.Z., Tammi, K., et al.: A new teaching–learning-based chicken swarm optimization algorithm. Soft. Comput. **24**(7), 5313–5331 (2020)
28. Rashedi, E., Rashedi, E., Nezamabadi-Pour, H.: A comprehensive survey on gravitational search algorithm. Swarm Evol. Comput. **41**, 141–158 (2018)
29. Zandevakili, H., Rashedi, E., Mahani, A.: Gravitational search algorithm with both attractive and repulsive forces. Soft. Comput. **23**(3), 783–825 (2019)
30. Rashedi, E., Nezamabadi-Pour, H., Saryazdi, S.: GSA: a gravitational search algorithm. Inf. Sci. **179**(13), 2232–2248 (2009)
31. Zheng, J., Gu, M., Pan, H., et al.: A fault classification method for rolling bearing based on multisynchrosqueezing transform and WOA-SMM. IEEE Access **8**, 215355–215364 (2020)
32. Bearing Data Center Website: Case Western Reserve University [DB/OL] [2017–6–20]. http://www.eecs.cwru.edu/laboratory/bearing.